Case Studies in Construction Materials 16 (2022) e01065

Contents lists available at ScienceDirect

Case Studies in Construction Materials

journal homepage: www.elsevier.com/locate/cscm

Corrosion resistance of multiscale polypropylene fiber-reinforced concrete under sulfate attack

Ninghui Liang [a,b,*], Jinwang Mao [a,b], Ru Yan [a,c], Xinrong Liu [a,b], Xiaohan Zhou [a,b]

[a] School of Civil Engineering, Chongqing University, Chongqing 400045, China
[b] National Joint Engineering Research Center for Prevention and Control of Environmental Geological Hazards in the TGR Area, Chongqing University, Chongqing 400045, China
[c] PowerChina Chengdu Engineering Corporation Limited, Chengdu, Sichuan 610072, China

ARTICLE INFO

Keywords:
Multiscale polypropylene fiber-reinforced concrete
Sulfate attack
Drying-wetting cycle
One-dimensional corrosion
Corrosion resistance mechanism

ABSTRACT

To study the corrosion resistance properties of multiscale polypropylene fiber-reinforced concrete (MPFRC) when subjected to sulfate attack, two types of fine polypropylene fiber (FPF) and one type of coarse polypropylene fiber (CPF) were selected for single doping or hybridization into concrete. A sodium sulfate solution (10 wt%) was used in the sulfate attack drying-wetting cycle. A one-dimensional SO_4^{2-} concentration distribution model was established. The corrosion resistance mechanism of polypropylene fiber-reinforced concrete (PFRC) was revealed based on concrete compressive strength tests, ion concentration tests, and micro tests under different sulfate attack ages. The results showed that PFRC maintained its integrity even after being subjected to sulfate attack. After 20 drying-wetting cycles, the MPFRC exhibited the highest compressive strength; the SO_4^{2-} concentration of the double-doped polypropylene fiber-reinforced concrete and MPFRC at 18 mm depth were 9.07% and 9.52% lower than those of the plain concrete and single-doped polypropylene fiber-reinforced concrete, respectively. The SO_4^{2-} concentration distribution model could well describe the SO_4^{2-} concentration distribution characteristics of the PFRC under one-dimensional sulfate attack. The diffusion coefficients (D) of the double-doped polypropylene fiber-reinforced concrete and MPFRC were 30.0% and 47.7% lower than that of plain concrete, respectively. Thus, among the concrete specimens used in this study, the MPFRC showed the best performance in terms of corrosion resistance.

1. Introduction

Concrete is a conventional building material widely used in the civil engineering industry. However, concrete underground structures—including highway tunnels, underwater tunnels, and underpasses—are vulnerable to sulfate attack from groundwater, soil, and seawater, which may cause these structures to deteriorate. Many concrete structures fail to reach their predetermined service life due to sulfate attack [1,2]. Thus, it is necessary to conduct studies to improve the corrosion resistance of concrete. The resistance of concrete against sulfate attack can be improved by using mineral admixtures to replace part of the cement. Common mineral admixtures include fly ash (FA), silica fume (SF), and slag. Sumer et al. [3] and Dong et al. [4] found that the addition of FA significantly increased the resistance of concrete to sulfate attack; the optimum FA dosages for fresh and precast concretes were found to be

* Corresponding author at: School of Civil Engineering, Chongqing University, Chongqing 400045, China.
E-mail address: liangninghui0705@163.com (N. Liang).

https://doi.org/10.1016/j.cscm.2022.e01065
Received 2 January 2022; Received in revised form 28 March 2022; Accepted 9 April 2022
Available online 12 April 2022

different. Canpolat et al. [5] and Yang et al. [6] found that concrete exhibited the strongest sulfate resistance when prepared with a 0.47 water-binder ratio, 6.0% entrained air, 5% SF, and 30% sand ratio. Ogawa et al. [7] and Yan et al. [8] found that cement blended with ground-granulated blast-furnace slag containing suitable amounts of limestone powder and calcium sulfate exhibited highly stable sulfate resistance. Thus, selecting and determining the mineral admixture type and dosage is complicated due to the existence of different types of concrete, curing conditions, and other conditions.

Incorporating fibers into concrete is another method for improving its corrosion resistance [9]. In recent years, fiber-reinforced concrete has been widely used because of its remarkable crack resistance, high strength, and toughness [10–12]. Fibers can be classified into natural, synthetic, and polymeric categories [13]. Natural fibers, such as açaí [14,15], curauá [16], and vegetable fibers [13] are chemically composed of organic materials; they undergo degradation due to the chemical decomposition of lignin and hemicellulose and are thus, unsuitable for enhancing the durability of concrete [17,18]. Synthetic and polymeric fibers have been widely used to enhance the corrosion resistance of concrete [19,20]. Moreover, studies have shown that fibers with different scales or properties possibly affect different stress stages, giving rise to a synergistic effect and resulting in a positive hybridization effect, thus further improving the performance of the concrete [21,22]. Considering the sulfate resistance of hybrid fiber-reinforced concrete, Bankir et al. [23] found that steel and propylene fibers were resilient against acid attacks; in addition, the sulfate resistance of hybrid fiber-reinforced concrete increased with the addition of steel, glass, and propylene fibers. Hou [24] found that concrete had the highest 7-day corrosion resistance coefficient when the amounts of basalt and polypropylene fibers added were 0.5 kg/m^3 and 0.3 kg/m^3, respectively. Wang et al. [25] found that incorporating different hybrid scales of steel fibers in cement-based composite materials could enhance their strength and toughness obviously, which had guiding significance for creating; this is important for developing high-performance cement-based composite materials. The current research on the sulfate resistance of hybrid fiber-reinforced concrete has mostly been focused on steel fibers. However, the application of steel fibers in concrete has limitations since steel is heavy and has low corrosion resistance. Recently, polypropylene fiber (PF) has been widely used for application in concrete, as it has several advantages over steel fiber, such as its light weight, low cost, high corrosion resistance, and compatibility with concrete. Researchers found that the hybridization of multiscale PF into concrete could improve its compressive strength [26], splitting tensile strength [27], crack resistance [28], fracture toughness [29], impermeability [30], and other properties; thus, studying its effect on the corrosion resistance of concrete is also important. However, there are insufficient reports describing the corrosion resistance properties of MPFRC.

In this study, three scales of PF (two types of FPF and one type of CPF) were selected for single doping or hybridization into concrete and were exposed to the drying-wetting cycle sulfate attack. Concrete specimens subjected to different drying-wetting cycles were used for compressive strength tests, ion concentration tests, scanning electron microscopy (SEM), energy-dispersive spectroscopy (EDS), and X-ray diffraction (XRD) tests. The corrosion resistance properties of the MPFRC were studied, a one-dimensional SO_4^{2-} concentration distribution model was established, and the corrosion resistance mechanism of the PFRC was revealed. This research is expected to be of great significance in the construction of highway tunnels, underwater tunnels, underpasses, and other underground engineering projects.

2. Experimental program

2.1. Materials and mix proportions

For this study, concrete of strength grade C30 was produced. The structure of the standard composite concrete and its control group consisted of the following materials: ordinary Portland cement of Grade 42.5R was used as a cementitious material; natural river sand was used as the fine aggregate (mud content is less than 2.1%, fineness modulus is 2.89) and artificial gravel with two types of particle sizes (5–10 mm and 10–20 mm) as the main aggregate; polycarboxylate superplasticizer with a water-reducing rate of 28% was used as the water-reducing admixture; running water was used for the mixing and curing of concrete; and other additives were used, including three different scales of PF: two kinds of FPF (FPF1 and FPF2) and one type of CPF. The physical and mechanical properties of FPF1, FPF2, and CPF are listed in Table 1, and their appearances are depicted in Fig. 1.

FPF alleviates the growth of microcracks while CPF is more effective in inhibiting the development of macrocracks [29]. Previous experimental data has shown that the optimum single amounts of FPF and CPF for this purpose were 0.9 kg m^{-3} and 6 kg m^{-3}, respectively [26–30]. To investigate the function of the PF in concrete, the proportion of the concrete mix was fixed, and only the content or mixing combination of PF was changed. The mix-proportion design was conducted according to the Chinese standard DL/T5330-2015 [31]. The mixing proportions of the C30 polypropylene fiber-reinforced concrete are listed in Table 2. Group A0 consisted of plain concrete and was considered as the control group; Groups A1, A2, and A3 contained only FPF1, FPF2, and CPF, respectively; Groups A4, A5, and A6 were blended with two types of PF while Groups A7 and A8 contained three types of PF.

Table 1
Physical and mechanical properties of polypropylene fibers.

Fiber	Diameter/ μm	Length/ mm	Tensile strength/ MPa	Elastic modulus/ GPa	Breaking elongation/%	Density/(g cm^{-3})	Recommended admixture/(kg m^{-3})
FPF1	26.1	19	641	10.6	26.0	0.91	0.9
FPF2	100	19	472	5.8	19.9	0.91	0.9
CPF	800	50	706	7.4	10.0	0.95	6.0

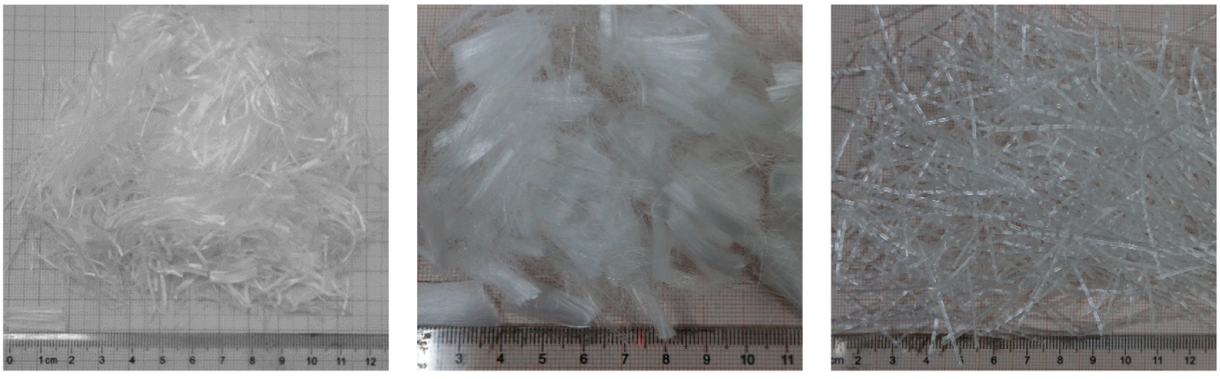

Fig. 1. Appearances of the polypropylene fibers.

Table 2
Mix proportion of C30 polypropylene fiber-reinforced concrete/(kg m^{-3}).

Group no.	PF content	Cement	Sand	Coarse aggregate	Water	Fiber content	Water-reducer/%
A0	/	380	701	1144	175	0	1
A1	FPF1	380	701	1144	175	0.9	1
A2	FPF2	380	701	1144	175	0.9	1
A3	CPF	380	701	1144	175	6.0	1
A4	FPF1 + CPF	380	701	1144	175	0.6 + 5.4	1
A5	FPF1 + CPF	380	701	1144	175	0.9 + 5.1	1
A6	FPF1 + CPF	380	701	1144	175	1.2 + 4.8	1
A7	FPF1 + FPF2 + CPF	380	701	1144	175	0.45 + 0.45 + 5.1	1
A8	FPF1 + FPF2 + CPF	380	701	1144	175	0.6 + 0.6 + 4.8	1

2.2. Specimen preparation

The specimens were cast in concrete molds (100 mm × 100 mm × 100 mm). They were removed from the molds after being subjected to natural curing for 24 h and were then cured in a standard curing room at 20 ± 2 °C and > 95% relative humidity for 28 days until testing. The specimens were used for surface feature observations, compressive strength tests, and ion concentration tests under different drying-wetting cycles. In each group, four specimens were prepared for testing under each sulfate attack age: three were used for the compression test and one for the sulfate ion concentration test. In total, 216 cubic specimens were cast. The mixing process of the fiber-reinforced concrete is shown in Fig. 2. The slump of the mixture was measured according to Chinese standard GB/T 50080-2016 [32], and the values are shown in Table 3.

2.3. Test methods

2.3.1. Drying-wetting cycle sulfate attack

Before subjecting the specimens to the drying-wetting cycle sulfate attack, epoxy resin AB glue was used to seal the entire concrete specimen except for a pair of opposite surfaces where the opposite side corrosion method was applied to study the one-dimensional sulfate attack law of SO_4^{2-}. At present, there is no uniform standard for a drying-wetting cycle sulfate attack. The concentration of sodium sulfate solution in a drying-wetting cycle sulfate attack is usually 1–15%, and the drying-wetting ratio is also variable [33–35]. In this study, a sodium sulfate solution (10 wt%) was used in the drying-wetting cycle sulfate attack. A drying-wetting cycle involves immersing the concrete samples in the sodium sulfate solution in a natural environment for 3 d and then drying the samples in air for 4 d for a drying-wetting ratio of 4:3. The experimental process is illustrated in Fig. 3. The duration of the drying-wetting cycle sulfate attack process was approximately five months and was divided into 20 drying-wetting cycles. The specimens were subjected to the 0 cycle (0 C), 4 cycles (4 C), 8 cycles (8 C), 12 cycles (12 C),16 cycles (16 C) and 20 cycles (20 C) drying-wetting sulfate attack. The

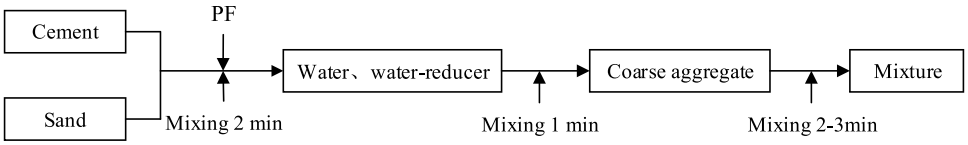

Fig. 2. Mixing process of fiber-reinforced concrete.

Table 3
Slump of mixture (mm).

Groups	A0	A1	A2	A3	A4	A5	A6	A7	A8
Slump	175	160	158	136	110	114	109	92	87

daily temperature and humidity data were recorded during this process, as shown in Fig. 4. The average relative humidity was 72.8% and the average temperature was 24.9 ℃ throughout the process.

2.3.2. Compressive strength test

In the beginning, the loading mode of the uniaxial compression test was stress control, followed by displacement control. Initially, a loading rate of 18 MPa/min was applied. When the uniaxial load exceeded 40% of the estimated compressive strength of the concrete, the loading mode was changed to the displacement control, and the loading rate was 0.5 mm/min until the specimen failed. The corrosion resistance coefficient was selected to evaluate the strength deterioration rule of the concrete subjected to the sulfate attack. The corrosion resistance coefficient was calculated using Eq. (1):

$$K = \frac{f_{ct}}{f_0} \tag{1}$$

where f_0 is the compressive strength of the concrete that was subjected to standard curing for 28 d and was not exposed to sulfate attack, f_{ct} is the concrete compressive strength under different drying-wetting cycle sulfate attack ages, and K is the corrosion resistance coefficient of the compressive strength. $K > 1$ indicates that the sulfate attack would positively effect the concrete compressive strength; $K < 1$ indicates that the sulfate attack would negatively effect the concrete compressive strength, causing the concrete to deteriorate significantly.

2.3.3. Ion concentration test

The SO_4^{2-} concentration at a specified depth of the concrete specimens under different drying-wetting cycles is a quantitative index for evaluating the corrosion rate. An engineering drilling machine was used to drill out core samples from the two opposite surfaces that were not sealed by the epoxy resin AB glue; the diameter of the core samples was 30 mm. Five slices, each having a thickness of 4 mm, were cut from each side. The samples were then ground into powder after drying them in an oven at 50 °C for 5 d. Finally, the powder was passed through a 0.074 mm aperture sieve to obtain a powder having a particle size no larger than 0.074 mm. The powder obtained from the same depth on both sides was evenly mixed in equal amounts with the sample of that layer. The SO_4^{2-} concentration was determined using the gravimetric method; Eq. (2) was used to calculate the mass fraction of SO_4^{2-}. The ion concentration testing process is illustrated in Fig. 5.

$$W_{SO_4^{2-}} = \frac{0.4116 \times (m_2 - m_1)}{m} \times 100\% \tag{2}$$

Where m is the mass of the powder (~ 1 g), m_1 is the mass of the filter membrane after drying in an oven at 60 ℃ for 24 h; m_2 is the mass of the filter membrane with precipitation after placing it in an oven at 60 ℃ for 48 h until a constant weight was achieved.

2.3.4. SEM, EDS and XRD analyses

The SEM, EDS, and XRD analyses revealed the corrosion resistance mechanism of the PFRC from a microscopic perspective. SEM was used to observe the changes in the microscopic morphology and crack propagation inside the concrete specimens after the sulfate attack. EDS and XRD were used to identify the main chemical products. Quattro SEM (Thermo Fisher Scientific) was used to observe the changes in the microscopic morphology inside the concrete. The device could also be used for EDS with an acceleration voltage of 15 kV. For different sulfate attack ages, the blocks with flat surfaces bonded with fibers were selected for SEM and EDS analyses. PANalytical X′pertPowder (Spectris Pte Ltd.) was used for the XRD test.

Fig. 3. Drying-wetting cycle process of specimens.

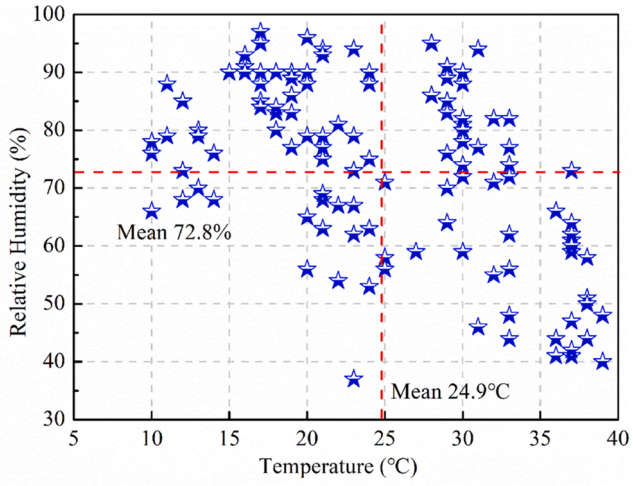

Fig. 4. Temperature and relative humidity during drying-wetting cycle.

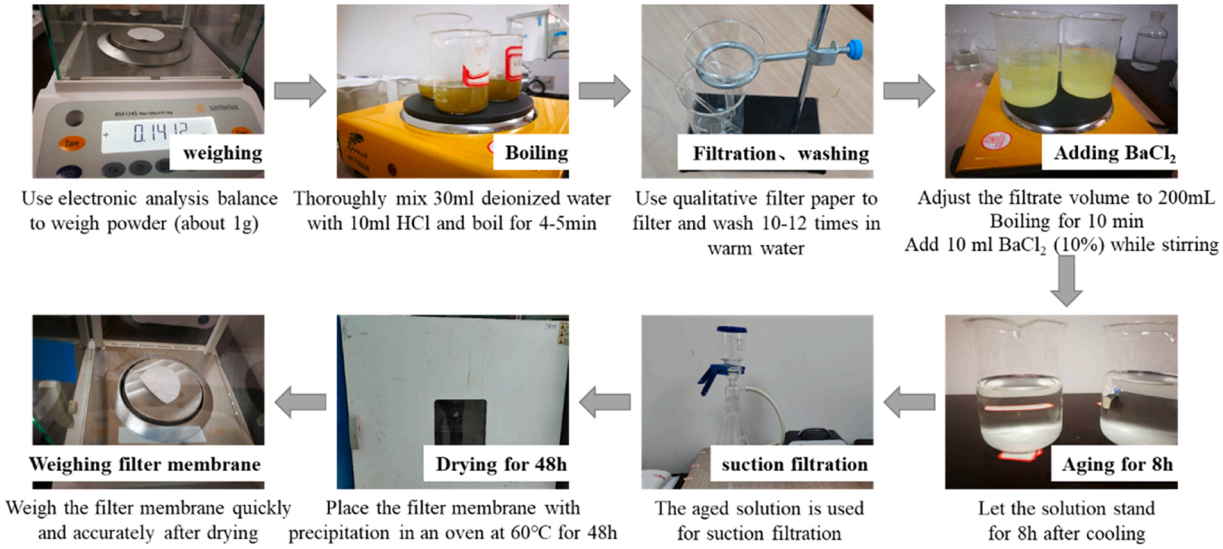

Fig. 5. Process of ion concentration testing.

3. Test results and discussion

3.1. Surface features

The surface features of plain concrete A0 and multiscale polypropylene fiber-reinforced concrete A8 that did not suffer from the sulfate attack are shown in Fig. 6(a) and (b). There were some micropores on the concrete surface; however, the specimens showed no edge cracking, edge off, or other macroscopic defects. Fig. 6(c) and (d) show the sulfate crystals on the surfaces of the concrete specimens under the drying cycles. The residual sodium sulfate solution on the surfaces evaporated quickly after being removed from the soaking solution; the surfaces dried 0.5 h later. After 1–3 h, white floc crystals began to appear at the edges of the specimens that gradually spread to the center. After drying for 12 h, white crystals were observed on the surface of the specimen, as shown in Fig. 6(c). The white floc crystals increased slightly 24 h later, as shown in Fig. 6(d), with no clear increase in the number of white crystals on the concrete surface.

Fig. 6(e)–(h) show the surface features of plain concrete A0 and the PFRCs A1, A6, and A8, respectively, after being subjected to 20 drying-wetting cycles. As the sulfate attack time increased, the deterioration of the surface of A0 increased gradually: part of the cement paste on the surface spalled, and the naked aggregate caused a sand phenomenon to occur. Compared to the A0, the surfaces of the PFRCs remained intact. Although the number and sizes of the pores on the PFRC surfaces showed an increasing trend, no clear deterioration phenomena, such as edge cracking or edge off, were observed, indicating that incorporating PF into the concrete could

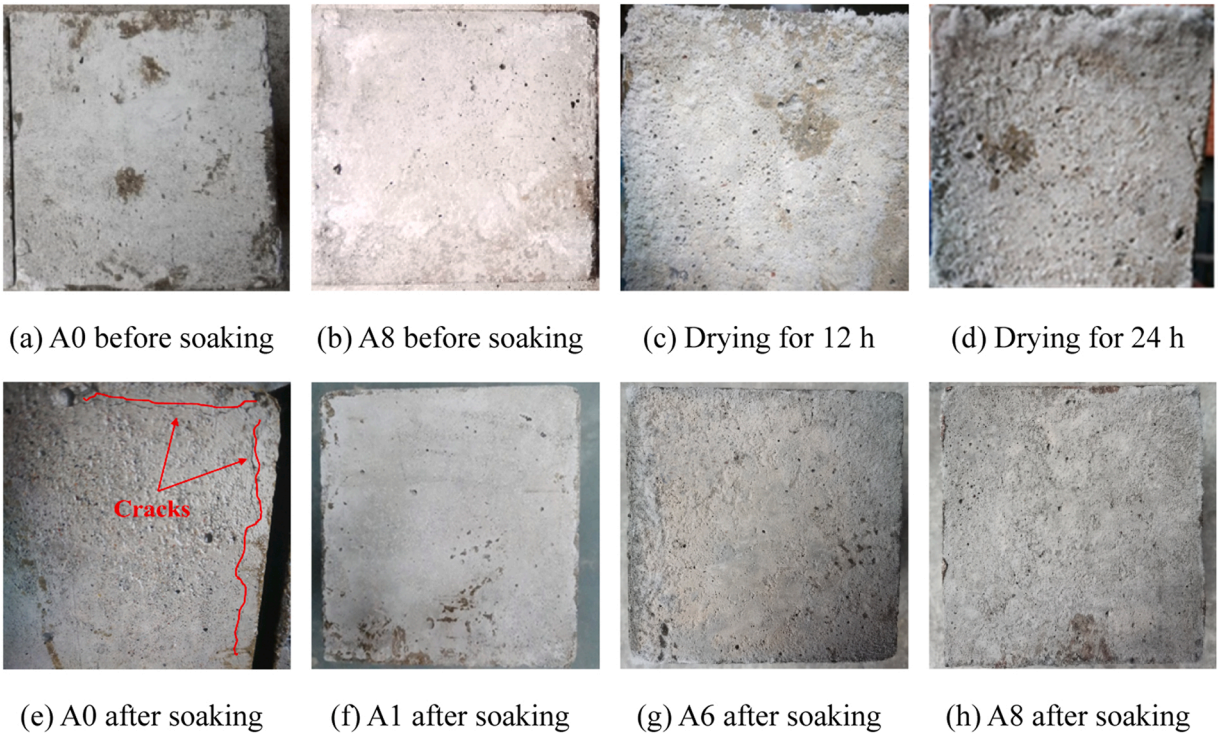

Fig. 6. Surface features of the specimens before and after sulfate attack.

maintain the integrity of the specimens.

3.2. Compression test

Fig. 7 shows the typical failure patterns of the concrete specimens when subjected to a drying-wetting cycle sulfate attack in the compressive strength test. Plain concrete appeared to have a "hoop effect", resulting in the specimens exhibiting two opposite conical failure surfaces [36], as shown in Fig. 7(a). Fig. 7(b)–(d) show the failure modes of the single-doped polypropylene fiber-reinforced concrete A1, double-doped polypropylene fiber-reinforced concrete A6, and multiscale polypropylene fiber-reinforced concrete A8, respectively. The integrities of the PFRC specimens, especially of the hybrid polypropylene fiber-reinforced concrete specimens A6 and A8, were better than that of plain concrete.

The sounds of concrete cracking and the fiber being pulled out were heard during the loading process. Multiple vertical cracks were observed on the specimens' surfaces. Although wider cracks developed at the edges, the concrete specimens did not disintegrate. Multiple fibers between the cracks could be observed, pulling together the concrete matrix; this effect was particularly significant in the case of CPF, as shown in Fig. 7(d). The bridging effect of the PF optimized the brittleness and improved the toughness of the concrete specimens. Fig. 8 shows the cubic compressive strengths and corrosion resistance coefficients of the PFRC specimens at different corrosion ages.

As seen in Fig. 8(a), the compressive strengths of the plain concrete and PFRCs can be divided into rising and falling stages

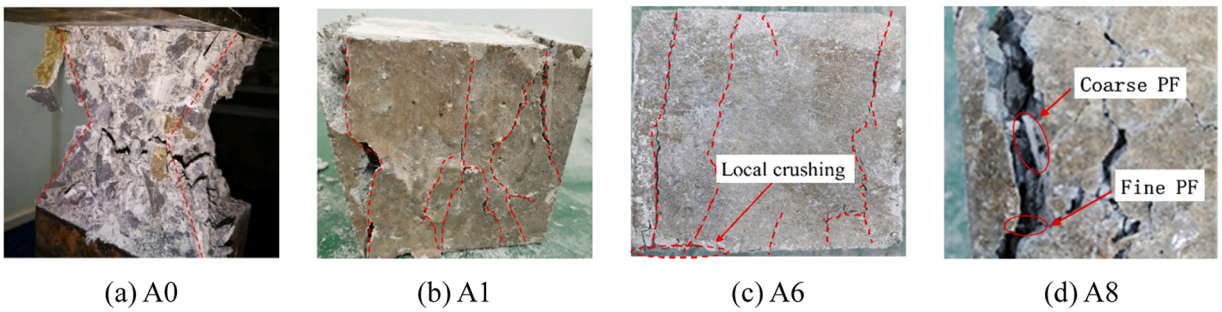

Fig. 7. Failure patterns of specimens.

considering the increasing sulfate attack ages, consistent with the compressive strength variation law of the concrete subjected to sulfate attack [37,38]. The strength of plain concrete A0 increased within eight cycles, whereas the rising period of the PFRCs reached ~ 12 cycles, indicating that the addition of PF delayed the strength reduction of the concrete when subjected to a drying-wetting cycle sulfate attack. After 20 drying-wetting cycles of sulfate attack, the compressive strengths of all the PFRC specimens were higher than that of plain concrete. The order of the compressive strengths of the specimens from highest to lowest was: multiscale polypropylene fiber-reinforced concrete > double-doped polypropylene fiber-reinforced concrete > single-doped polypropylene fiber-reinforced concrete > plain concrete. This order indicates that the addition of PF, especially the hybridization of multiscale PF, into concrete could improve its compressive strength. As seen in Fig. 8(b), after 20 drying-wetting cycles, the corrosion resistance coefficients of the plain concrete A0 and single-doped fine PFRC A2 were lower than 1.0 whereas those of the double-doped PFRC and MPFRC were all greater than 1.0, indicating that the addition of PF slowed the damage rate of the concrete when subjected to the sulfate attack and that the effect of the hybrid PF was more clear in this regard.

3.3. Sulfate ion content

The SO_4^{2-} concentration test results for A0, A1, A3, A6, and A8 under different sulfate attack ages are shown in Fig. 9. The sulfate ion content of the plain concrete that did not suffer from the sulfate attack was 0.806%. It was assumed that the initial sulfate ion

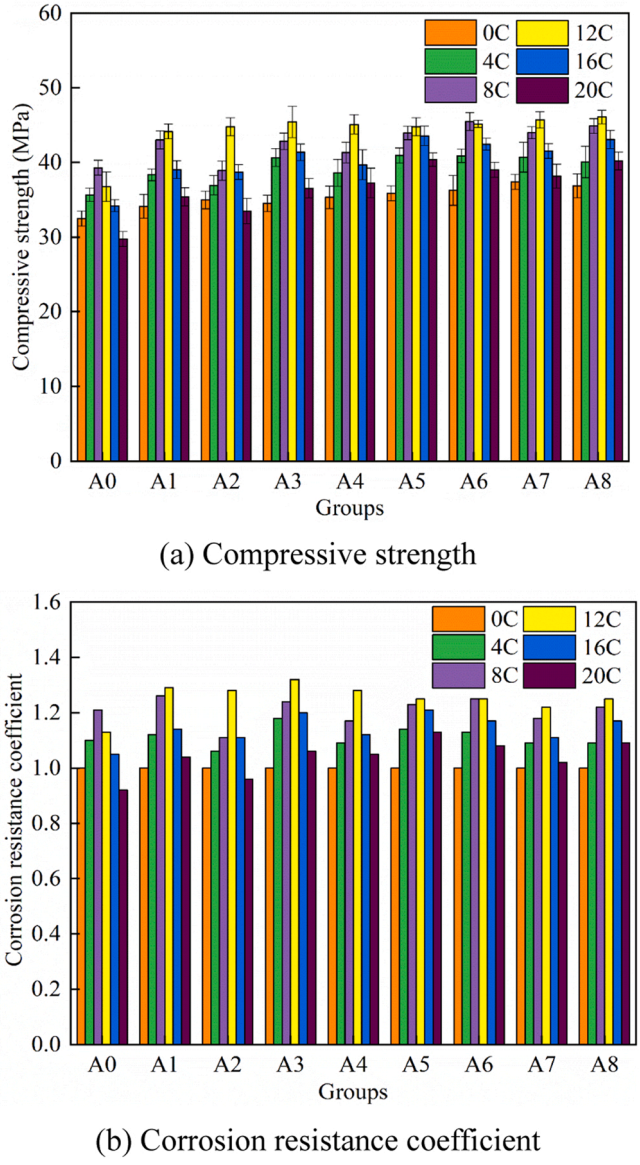

Fig. 8. Compressive strengths and corrosion resistance coefficients of the specimens under different corrosion ages.

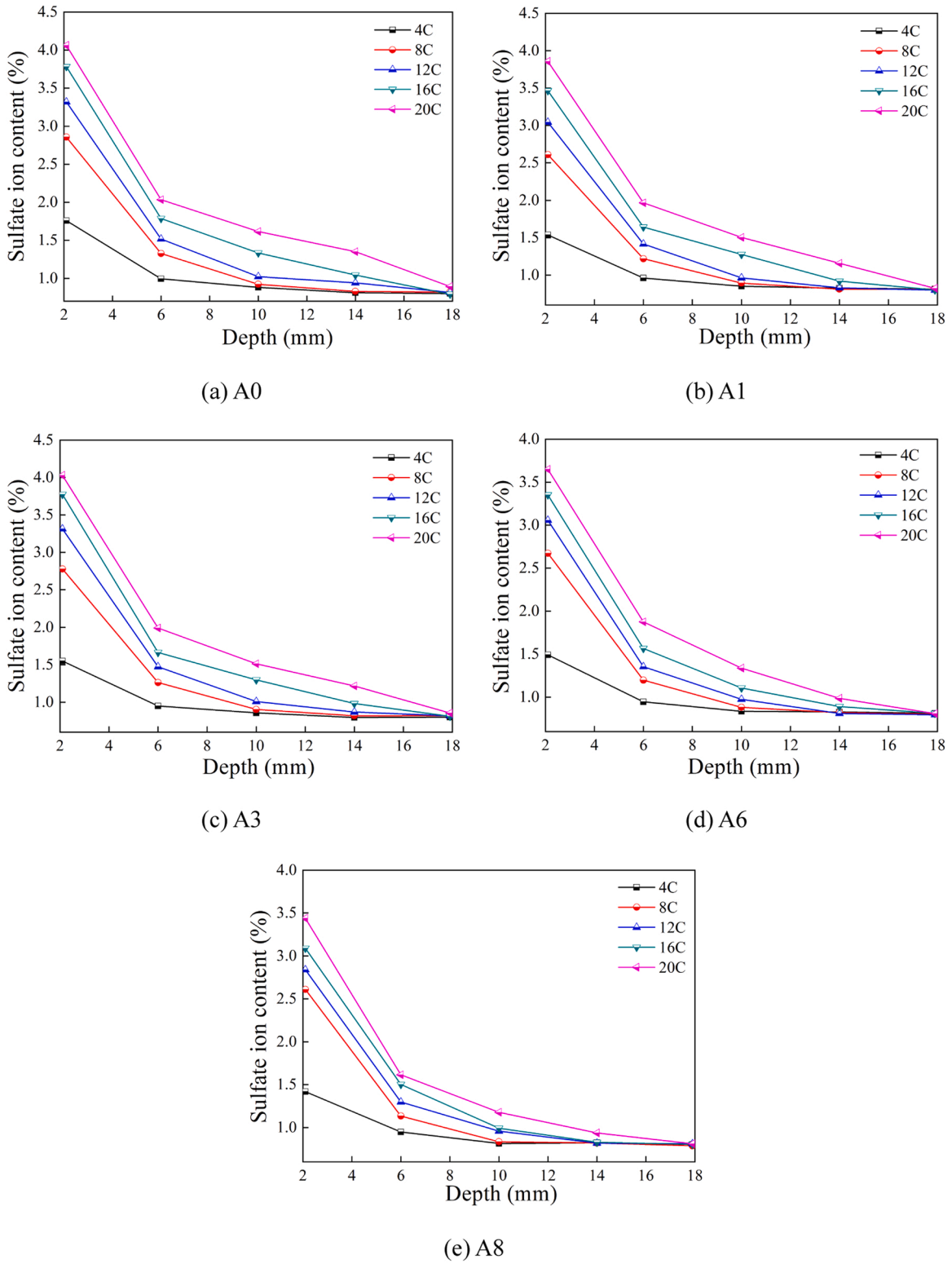

Fig. 9. Sulfate ion concentrations under different sulfate attack ages.

concentration of each concrete specimen was 0.806%, distributed evenly throughout the specimen.

As seen in Fig. 9, the variation law of SO_4^{2-} concentration in each group was consistent. As the depth increased, the SO_4^{2-} concentration decreased. When the depth was constant, the concentration increased with increasing drying-wetting cycles. After four drying-wetting cycles, the SO_4^{2-} concentration in plain concrete at a depth of 2 mm was 1.760%, decreasing to 0.882% at a depth of 10 mm, indicating that the sulfate attack depth was ~ 10 mm. After 20 drying-wetting cycles, the SO_4^{2-} concentration in plain concrete increased by 2.302% at a depth of 2 mm and by 0.734% at a depth of 10 mm. At a depth of 18 mm, the concentration was 0.893%, 0.087% higher than the initial sulfate ion concentration, indicating that the sulfate attack depth exceeded 18 mm. Under the same conditions, the SO_4^{2-} concentrations of the PFRCs were lower than that of plain concrete, indicating that incorporating PF into the concrete could improve its resistance to the sulfate attack and delay the corrosion rate of SO_4^{2-}. After four drying-wetting cycles, the SO_4^{2-} concentrations at a depth of 2 mm for A1 and A3 were 1.536% and 1.549%, respectively; those at a depth of 10 mm were 0.852% and 0.857%, respectively. Thus, the sulfate attack depth was ~ 10 mm. It is also evident from the results that the resistance of the single-doped fine PFRC to the sulfate attack was slightly better than that of the single-doped coarse PFRC. After 20 drying-wetting cycles, the sulfate attack depths of A1 and A3 were approximately 18 mm; their SO_4^{2-} concentrations at a depth of 10 mm were 1.503% and 1.512%, respectively, 0.113% and 0.104% lower than that of plain concrete, respectively. For the double-doped PFRC A6

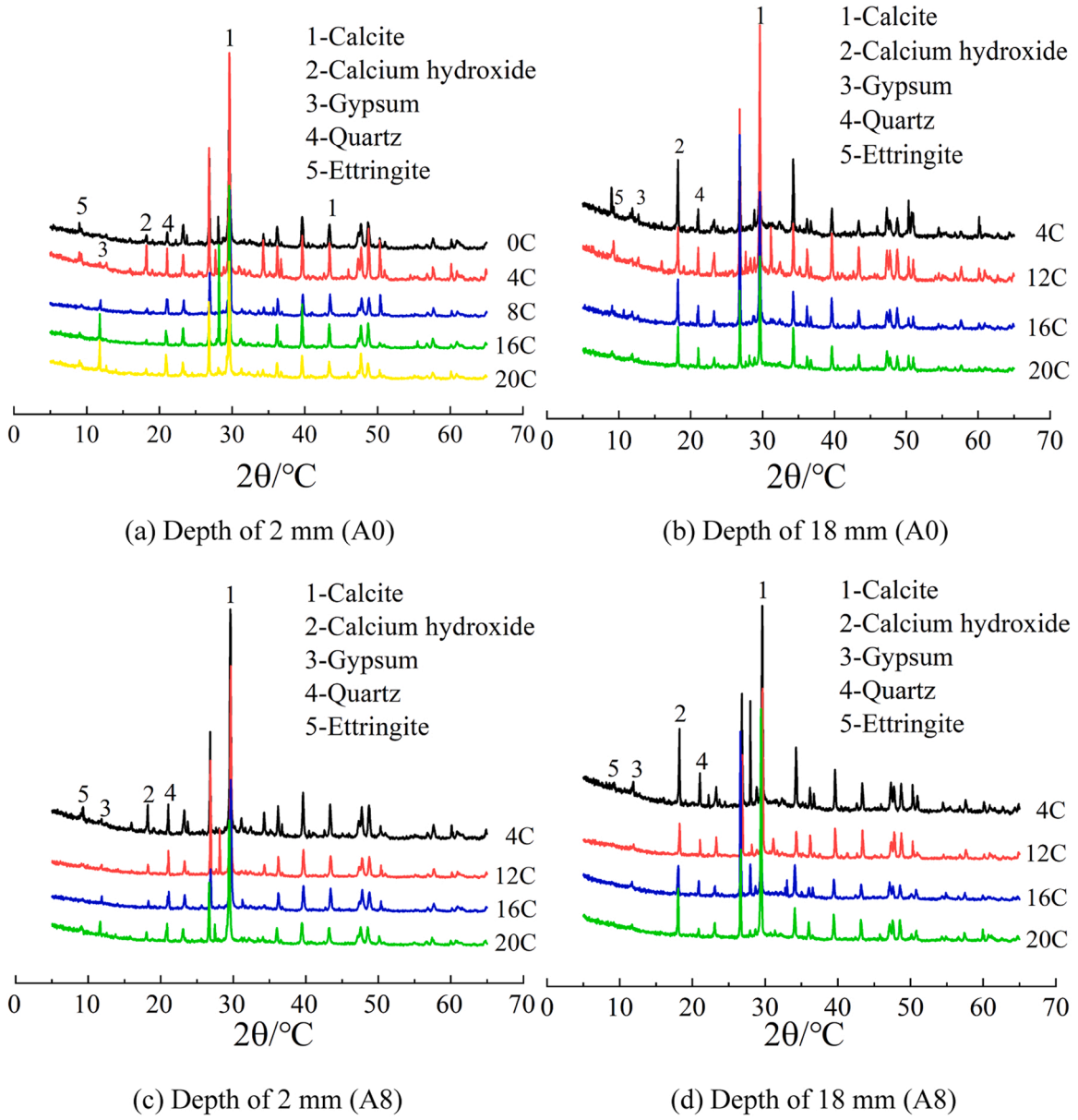

Fig. 10. XRD patterns of A0 and A8 under different sulfate attack ages.

and MPFRC A8, the SO_4^{2-} concentrations were lower than those of the other groups. After 20 drying-wetting cycles, the SO_4^{2-} concentrations at a depth of 18 mm for A6 and A8 were 0.812% and 0.808%, respectively, 9.07% and 9.52% lower than that of A0. These values were close to the initial sulfate ion concentration. Thus, of all the specimens, incorporating different hybrid scales of PF into the concrete had the most significant effect on improving its resistance to sulfate attack.

3.4. Corrosion resistance mechanism of PFRC

For this experiment, we considered the plain concrete A0 and MPFRC A8 as examples. Their chemical compositions at the depths of 2 mm and 18 mm under different sulfate attack ages were analyzed, as shown in Fig. 10.

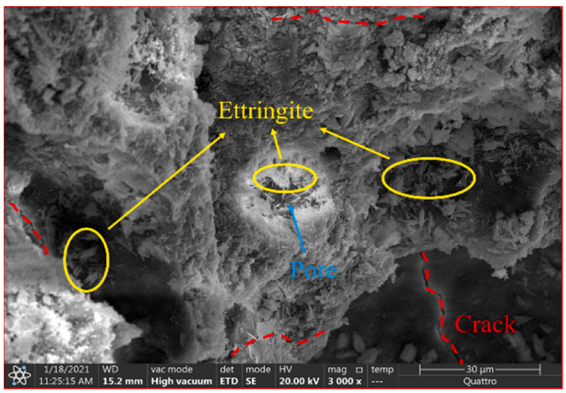

(a) Accumulation of ettringite

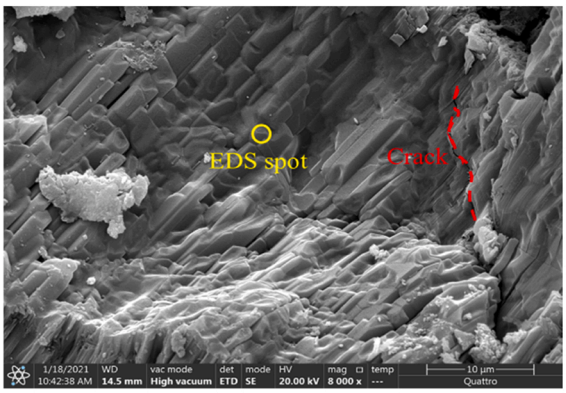

(b) SEM image of gypsum

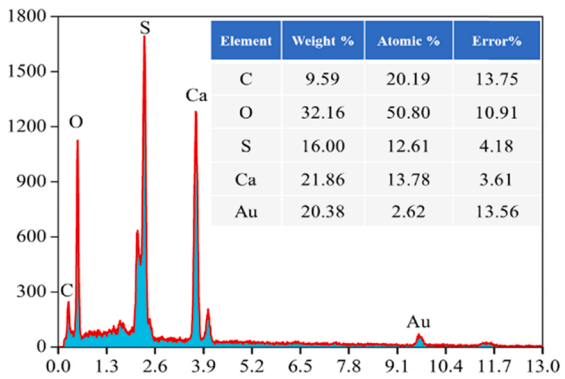

Element	Weight %	Atomic %	Error%
C	9.59	20.19	13.75
O	32.16	50.80	10.91
S	16.00	12.61	4.18
Ca	21.86	13.78	3.61
Au	20.38	2.62	13.56

(c) EDS spectrum of gypsum

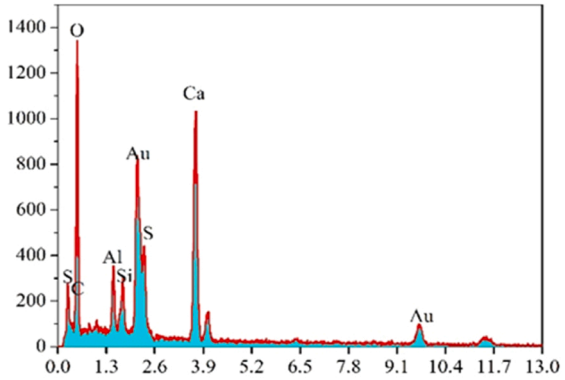

(d) EDS spectrum of ettringite

Element	Weight %	Atomic %	Net Int.	Error %
C	7.66	17.34	56.77	12.83
O	34.25	58.17	398.19	10.47
Al	2.35	2.36	114.33	8.81
Si	1.73	1.67	98.29	9.10
S	4.45	3.77	191.68	7.69
Ca	18.22	12.35	584.40	4.16
Au	31.34	4.32	89.20	11.57

(e) Element proportion of ettringite

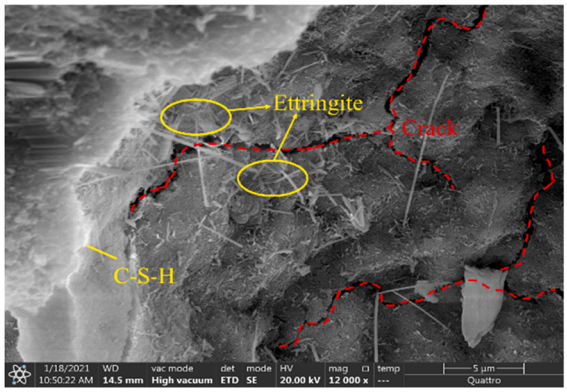

(f) After 20 drying-wetting cycles.

Fig. 11. SEM images and EDS spectra of plain concrete before and after sulfate attack.

The results of the XRD analysis showed that ettringite and gypsum were obtained as the main chemical corrosion products of concrete when subjected to a drying-wetting cycle sulfate attack. Due to the presence of ettringite produced by cement hydration, weak diffraction peaks of ettringite were observed in the case of the concrete samples that did not suffer from the sulfate attack. With an increase in the number of drying-wetting cycles, an increasing amount of ettringite was generated, indicated by the observation of clear diffraction peaks of ettringite. Under the same sulfate attack age, the diffraction peak intensity of ettringite in the case of A8 was much weaker than that in the case of A0 at the same depth, implying that the addition of PF delayed the corrosion rate of SO_4^{2-}. Calcium hydroxide (CH) was continuously consumed with increasing sulfate attack age, indicated by a significant decrease in the CH diffraction peak, especially in the case of plain concrete A0. After 20 drying-wetting cycles, there was no clear CH diffraction peak at the depth of 2 mm inside the sample; the consumption of CH resulted in a decrease in the concrete alkalinity. In contrast, for A8, there was still a clear CH diffraction peak at the 2 mm depth even after 20 cycles. The diffraction peak of CH decreased slightly at 18 mm depth for A0 and A8 after 20 drying-wetting cycles, indicating that SO_4^{2-} had already invaded the concrete deeply; however, it did not cause significant corrosion. Thus, the XRD results were in agreement with the results of the sulfate ion concentration test, proving that incorporating different scales of PF into the concrete could significantly improve its resistance to sulfate attack from a microscopic perspective.

The microcosmic appearance of the plain concrete A0 before and after the sulfate attack drying-wetting cycles, and the EDS analysis results of the corrosion products are shown in Fig. 11. At the initial stage of sulfate attack, corrosion products were easily deposited and accumulated in the initial pores and cracks inside the concrete, as shown in Fig. 11(a). This did not damage the specimens; rather, it improved the compactness of the concrete matrix, which was the main reason for the improvement of the concrete compressive strength. The microscopic morphologies of the two main corrosion products could be described as short and columnar, and needle-like. Fig. 11(b) and (c) show the microscopic morphology and EDS analysis results, respectively, of the short, columnar crystals. Their main elements were Ca, S, and O, indicating that they were gypsum crystals. The EDS analysis results of the needle-like crystals are shown in Fig. 11(d) and (e), mainly comprising O, S, Si, Ca, and Al, indicating that they were ettringite crystals. Fig. 11(f) shows the corrosion products observed near the microcracks inside the concrete after 20 drying-wetting cycles. Studies have shown that the solid-phase volumes of ettringite and gypsum in concrete would increase by ~ 94% and ~ 124%, respectively [39] when subjecting concrete to sulfate attack. Gypsum and ettringite were deposited and accumulated in the initial pores and microcracks. Gradually, an increasing number of crystals were accumulated, generating an expansion stress. When the expansion stress exceeded the tensile strength of the concrete, more microcracks were generated and developed, leading to the initial damage.

A hollow effect exists in the drying-wetting cycle sulfate attack of concrete [40]. During this process, the cement gel was continuously consumed, the porosity and permeability of the concrete increased, and the cementing materials on the concrete surface peeled off slightly, resulting in a loss of quality and reduction in the bearing capacity. As shown in Fig. 12(a), ettringite accumulated in the initial pores and cracks inside the PFRC, and the position of accumulation was the same as that in plain concrete because the addition of PF could not completely prevent the chemical reaction between the sodium sulfate solution and cement. As seen in Fig. 12 (b), the hollow effect resulted in the development of more small holes in the concrete after the sulfate attack. When the concrete was destroyed under an external force, one end of the fiber was pulled off or pulled out, and the other end was firmly embedded in the concrete matrix, indicating that the adhesive capacity between the PF and concrete matrix was adequate. Splitting [27] and uniaxial tensile tests [41] revealed that the PF at the fracture section could withstand the loads. The bridging effect of the PF enabled the transfer of loads to the uncracked parts, which dispersed the stress concentration and constrained the propagation of the cracks. Simultaneously, the adhesion and mechanical interaction between the fibers and concrete matrix prevented the fibers from being pulled off or pulled out. Thus, the tensile strength of the PFRC improved, and the strength ratio was in the range ~ 1.09–1.27. The degree of improvement was related to the fiber content and fiber type, and the advantages of the MPFRC were more clear in this regard. The addition of the PF enhanced the tensile property of concrete and restrained the opening of cracks ensuring that the concrete matrix could withstand greater expansion stress; the width of the cracks was limited, blocking the passage of the sodium sulfate solution into

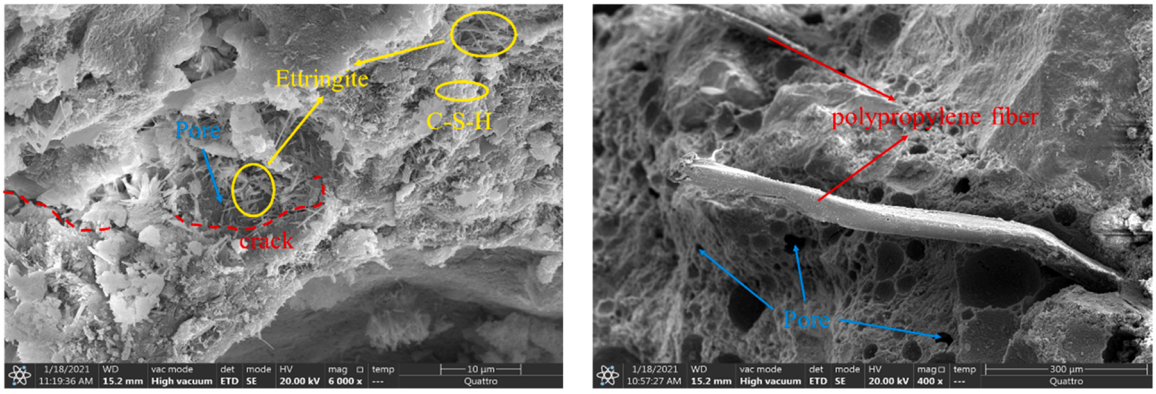

Fig. 12. SEM image of polypropylene fiber-reinforced concrete after sulfate attack.

the concrete and slowing the corrosion rate of SO_4^{2-}. This was one of the main reasons for the corrosion resistance of the PFRC being higher than that of plain concrete.

In addition to the chemical corrosion, physical corrosion occurred under the drying-wetting cycle sulfate attack. Physical corrosion was dominated by sulfate crystallization, and its macroscopic morphology is shown in Fig. 5(c) and (d). Fig. 13(a) shows the XRD pattern of sulfate crystallization. The main components were thenardite (Na_2SO_4) and mirabilite ($Na_2SO_4{\cdot}10H_2O$), with the amount of Na_2SO_4 being greater. Fig. 13(b) shows the microscopic morphology of sulfate crystallization, described as a cake structure with a diameter in the range of 0.2–2 μm. In the drying cycle, the expansion stress generated by sulfate crystallization can be considered the loading process. In the wetting cycle, the dissolution of sulfate crystallization occurs considered the unloading process. The process of repeated generation and dissolution of sulfate crystallization gives rise to the fatigue process of repeated loading and unloading, accelerating the initiation and expansion of microcracks inside the concrete [42]. Prior research has shown that the addition of PF could improve the fatigue resistance of the concrete matrix [43]; therefore, the addition of PF should also enable the concrete to resist the fatigue load of sulfate crystallization in the drying-wetting cycles and increase the corrosion resistance of the PFRC.

In addition, incorporating PF into concrete should enhance the anti-permeability of the concrete matrix. Through porosity and nuclear magnetic resonance tests, the porosities, most probable pore sizes, and critical pore radii of A0, A3, A6, and A8 were determined, as shown in Table 4. The porosities of the PFRCs were slightly higher than that of plain concrete, consistent with the SEM image. However, the proportion of the pores greater than 100 nm in plain concrete A0 was much higher than those in the PFRCs; the pores proportion of MPFRC A8 was the smallest at 26.87%.

Based on the water permeability of the pores, Wu et al. [44] defined pores larger than 100 nm as harmful pores, significantly influencing the anti-permeability; pores smaller than 100 nm were defined as harmless pores, with negligible influence on the anti-permeability. Thus, it is evident from the obtained results that incorporating the PF into concrete, especially the hybridization of multiscale PF, optimized the concrete pore structure, reduced the proportion of harmful pores, and improved the proportion of harmless pores. This could, in turn, reduce the rate of SO_4^{2-} invasion into concrete, corresponding to the smaller sulfate ion concentration of PFRC with the same corrosion age and depth (as shown in Fig. 9). The incorporation of PF into concrete was able to refine its pore size. The most probable pore size of the plain concrete A0 was 43.21 nm while those of the PFRCs were lower, especially that of A8, which had a value of 32.32 nm, 25.20% lower than that of A0. Additionally, the critical pore radius was also optimized; its value for A0 was 59.02 nm while it was 42.42 nm for A8. The critical pore radius reflects the connectivity of the pores and the tortuosity of the permeability path to some extent. As shown in Fig. 14, the PF present inside the concrete inhibited the development of cracks while also blocking the cracks, significantly reducing the connectivity of the concrete internal pores and increasing the tortuosity of the permeability path. Thus, the anti-permeability and corrosion resistance of the PFRC were significantly improved.

3.5. SO_4^{2-} concentration distribution model of PFRC

The distribution of the SO_4^{2-} concentration reflects the diffusion reaction characteristics of sulfate inside concrete, which is the bridge connecting the diffusion reaction of sulfate with the expansion and cracking of concrete. The diffusion coefficient of SO_4^{2-} can accurately reflect the concentration distribution of sulfate inside concrete. Thus, it is important to establish a reliable sulfate distribution model to accurately obtain the SO_4^{2-} diffusion coefficient for studying the corrosion resistance of concrete [45]. In this study, a one-dimensional SO_4^{2-} concentration distribution model of the PFRC subjected to sulfate attack was established based on Fick's law and the mass conservation law.

Fig. 15 shows a diagram of one-dimensional sulfate attack, consistent with the one-dimensional sulfate attack test. We considered an internal microelement $[x, x + \Delta x]$ as the research object. According to the mass conservation law: the liquid SO_4^{2-} content at the microelement level = the input of SO_4^{2-} − the output of SO_4^{2-} − the consumption of SO_4^{2-}.

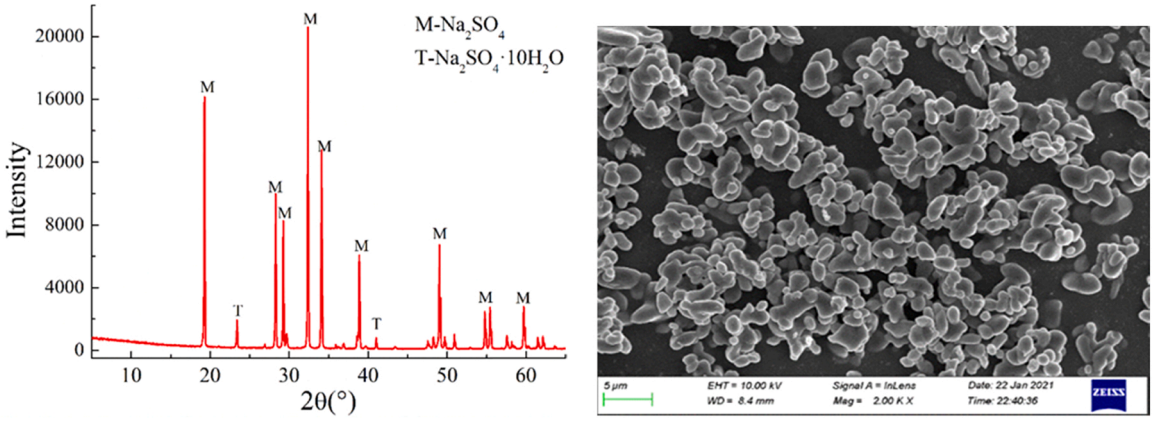

(a) XRD pattern (b) SEM image

Fig. 13. XRD pattern and SEM image of sulfate crystallization.

Table 4
Test parameters of pore structure [30].

Group	Porosity/%	Most probable pore size/nm	Critical pore radius/nm	Pore smaller than 100 nm/%	Pore larger than 100 nm/%
A0	3.314	43.21	59.02	54.72	43.22
A3	3.282	40.12	54.15	54.30	35.27
A6	3.504	34.68	48.33	59.94	29.67
A8	3.649	32.32	42.42	56.57	26.87

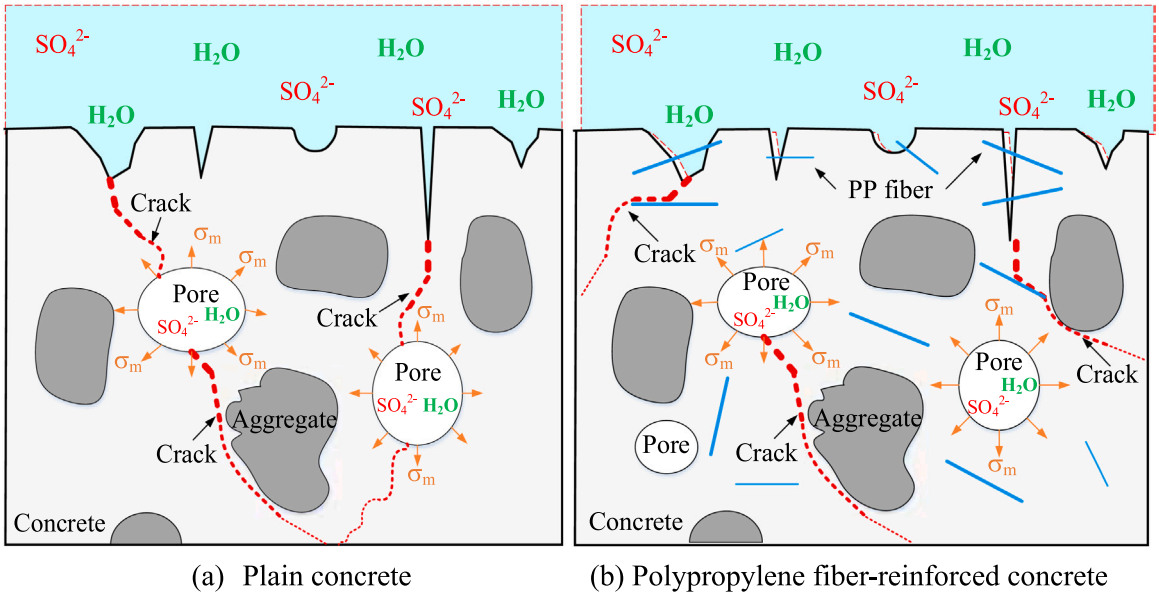

Fig. 14. Schematic diagrams of the sulfate attack mechanism.

It was assumed that the concrete matrix was isotropic and that the initial SO_4^{2-} concentration of the concrete was evenly distributed. Based on Fick's law, the following relation can be obtained:

$$C_x = -D\frac{\partial C(x,t)}{\partial x} \tag{3}$$

where C_x is the SO_4^{2-} content of section x, D is the diffusion coefficient of SO_4^{2-}, and "–" indicates that SO_4^{2-} diffuses from a region of high concentration to a region of low concentration. Therefore, the total content of SO_4^{2-} in the solid and liquid phases, m_1, is:

$$m_1 = D\int_t^{t+dt} dt \int_x^{x+dx} \frac{\partial^2 C(x,t)}{\partial x^2} \cdot Sdx \tag{4}$$

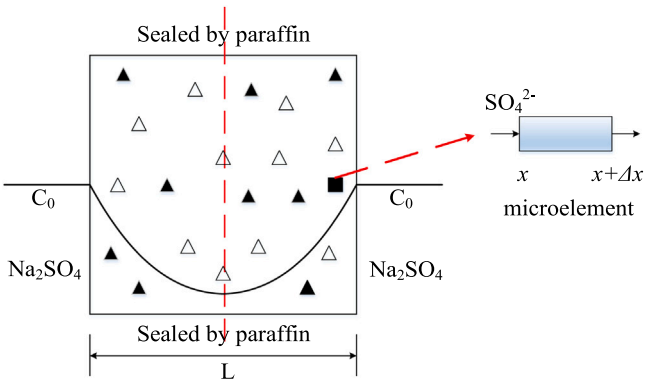

Fig. 15. Illustration of one-dimensional sulfate attack.

A previous study showed that the concentration of SO_4^{2-} had an important effect on the chemical reactions of sulfate attack [46]. The formation of ettringite under the action of sulfate is considered a first-order chemical reaction. Therefore, based on the first-order reaction principle, the following equation was obtained:

$$\frac{\partial C_{SO_4^{2-}}}{\partial t} = k \cdot C\left(x,t\right) \tag{5}$$

where k is the rate coefficient (s^{-1}) determined by a specific reaction at a specific temperature. The consumption of SO_4^{2-} by the microelement (m_2) is given by:

$$m_2 = \int_t^{t+dt} \frac{\partial C_{SO_4^{2-}}}{\partial t} dt \int_x^{x+dx} Sdx = k \int_t^{t+dt} dt \int_x^{x+dx} C(x,t) \cdot Sdx \tag{6}$$

According to Eqs. (4) and (6), the increment of SO_4^{2-} in the liquid phase (Δm) at the microelement within time dt is

$$\Delta m = \int_x^{x+dx} S[C(x,t+dt) - C(x,t)]dx = \int_t^{t+dt} dt \int_x^{x+dx} \frac{\partial C(x,t)}{\partial t} \cdot Sdx \tag{7}$$

According to Eq. (7):

$$D \int_t^{t+dt} dt \int_x^{x+dx} \frac{\partial^2 C(x,t)}{\partial x^2} \cdot Sdx - k \int_t^{t+dt} \int_x^{x+dx} C(x,t) Sdtdx = \int_t^{t+dt} dt \int_x^{x+dx} \frac{\partial C(x,t)}{\partial t} \cdot Sdx \tag{8}$$

where $\frac{\partial^2 C(x,t)}{\partial t}$ is the rate of change of the SO_4^{2-} concentration in the liquid phase at a certain depth inside the concrete. Krajcinovic et al. [47] found that the effect of diffusion coefficient on chemical reaction was not significant, but the effect of chemical reaction rate was very significant. The accumulation rate of SO_4^{2-} was negligible compared with the consumption rate of the chemical reaction. Considering $\alpha = \sqrt{k/D}$, Eq. (8) can be simplified as follows.

$$\frac{\partial^2 C(x,t)}{\partial x^2} - \alpha^2 C\left(x,t\right) = 0 \tag{9}$$

The general solution to Eq. (9) could be described as: $C(x,t) = \beta_1 e^{\alpha x} + \beta_2 e^{-\alpha x}$. When $x = 0$, $C = C_s(t)$, indicating that the SO_4^{2-} concentration at the concrete's surface is a function of time. When $x = h$ (h is the maximum diffusion depth), $C = C_0$, where C_0 is the initial SO_4^{2-} concentration of concrete. Therefore, the SO_4^{2-} concentration distribution at a specified depth inside concrete at any time can be expressed by Eq. (10) according to the boundary conditions:

$$C\left(x,t\right) = \begin{cases} \dfrac{[C_s(t)\sinh[\alpha(h-x)] + C_0 \sinh(\alpha x)]}{sinh(\alpha h)}; x \le h \\ C_0; x \ge h \end{cases} \tag{10}$$

where $\sinh(x)$ is the hyperbolic sine function given by: $\sinh(u) = \frac{e^u - e^{-u}}{2}$.

Eq. (10) was used to fit the ion concentration test results. The surface sulfate concentration value and α value of each specimen group at different drying-wetting cycles were obtained. The fitting results are presented in Table 5. The correlation coefficients R^2 were all greater than 0.9, indicating that Eq. (10) was suitable for describing the SO_4^{2-} concentration distribution characteristics of the PFRC under one-dimensional sulfate attack.

As seen in Table 5, the α value of each group changed with the change in corrosion age, i.e., the diffusion coefficient D changed with the corrosion time. By fitting the test data, Barovsky et al. [48] found that the k values under different conditions ranged from 2.9 to 3.1×10^{-7}/s. In this study, $k = 3 \times 10^{-7}$/s was used to quantitatively analyze the time variation law of D; the results are shown in Fig. 16.

As seen in Fig. 16, the diffusion coefficient D first decreased and then increased. At the initial stage of the sulfate attack, the diffusion coefficient of the concrete decreased rapidly due to the hydration reaction occurring inside the concrete and the filling effect of the corrosion products on the micropores, making the concrete more compact and slowing the diffusion rate of SO_4^{2-}. As the sulfate attack time increased, an increasing number of microcracks were produced, and C-S-H was consumed continuously, resulting in an increase in the diffusion coefficient in the latter stage. The diffusion coefficient of plain concrete A0 was larger than those of the PFRCs for all sulfate attack ages, indicating that A0 was the most vulnerable to sulfate attack. The diffusion coefficients of A1, A3, A6, and A8 for 20 drying-wetting cycles were 15.7%, 19.0%, 30.0%, and 47.7% lower than that of A0, respectively. The results show that incorporating PF, especially the hybridization of multiscale PF, into concrete could effectively reduce the diffusion coefficient of SO_4^{2-} and delay the corrosion rate of sulfate.

4. Conclusions

In this study, plain concrete and PFRC specimens were subjected to a drying-wetting cycle sulfate attack to study the corrosion resistance properties of the MPFRC and reveal the corrosion resistance mechanism of the PFRC. The SO_4^{2-} concentration distribution model under one-dimensional sulfate attack was also established. The main conclusions are as follows:

Table 5
Fitting results of each group specimen at different drying-wetting cycles.

Cycles (C)	Group	Corrosion depth (mm)	$C_{surface}$ (t)	a	R^2
4	A0	11.0	2.406	141.59	0.980
	A3	10.5	2.027	157.01	0.987
	A3	10.5	2.069	163.23	0.986
	A6	10.0	1.980	160.52	0.993
	A8	9.0	1.814	171.98	0.999
8	A0	12.0	4.147	194.09	0.993
	A3	11.0	3.908	209.87	0.995
	A3	11.0	4.206	214.60	0.995
	A6	10.5	3.834	225.36	0.982
	A8	10.0	3.712	241.69	0.991
12	A0	15.0	4.741	186.40	0.985
	A3	14.0	4.411	192.71	0.993
	A3	14.5	4.833	196.28	0.990
	A6	12.0	4.576	208.81	0.989
	A8	11.0	4.241	207.90	0.989
16	A0	17.0	5.047	157.02	0.969
	A3	15.5	4.688	162.53	0.974
	A3	16.0	5.191	171.96	0.966
	A6	14.5	4.737	181.04	0.988
	A8	14.0	4.403	183.69	0.996
20	A0	20.5	5.005	124.84	0.941
	A3	18.0	4.921	135.99	0.968
	A3	18.5	5.153	138.75	0.959
	A6	16.5	4.823	148.97	0.986
	A8	15.0	4.765	172.55	0.981

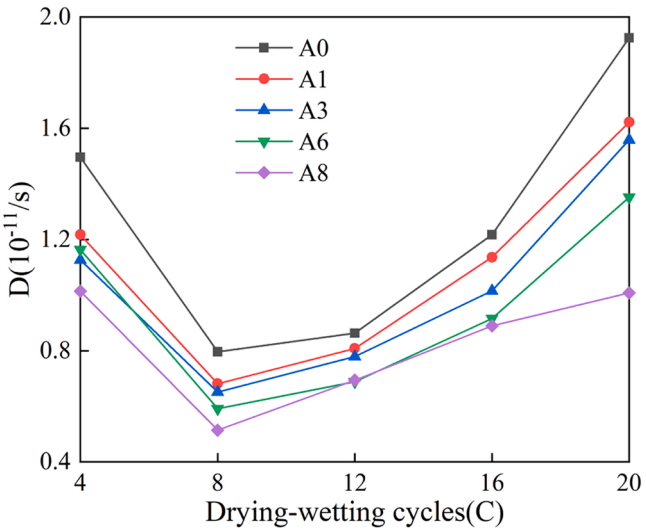

Fig. 16. Time variation law of the diffusion coefficient.

(1) After being subjected to 20 drying-wetting cycles of sulfate attack, plain concrete showed clear signs of deterioration while the PFRCs remained intact; the MPFRC exhibited the highest compressive strength. At a specified depth, the SO_4^{2-} concentrations of the PFRCs were lower than that of plain concrete.
(2) The bridging effect of randomly distributed PFs improved the tensile properties of the concrete. The concrete could bear larger expansion stress, inhibit the initiation, development, and penetration of internal cracks, resist the fatigue load of sulfate crystallization in the drying-wetting cycles, and optimize the pore structure. In this regard, the hybridization of different-scale fibers into concrete was the most effective.
(3) The established SO_4^{2-} concentration distribution model was suitable for describing the SO_4^{2-} distribution characteristics of the PFRCs under one-dimensional sulfate attack. The diffusion coefficients of A1, A3, A6, and A8 lower than that of A0, respectively, indicating that the corrosion resistance of the PFRCs, especially those of the MPFRC, were much better than that of plain concrete. This study would have great significance in improving concrete engineering in a sulfate-attack environment.

Funding

This work was supported by the Mechanical Effect and Safety Analysis of Severely Damaged Tunnel Renovation Process (Grant no. H20210058).

Declaration of Competing Interest

The authors declare that they have no known competing financial interests or personal relationships that could have appeared to influence the work reported in this paper.

References

[1] F.S. Ebrahim, S.A. Zohreh, B. Massoud, S. Mostafa, Assessing the hydrogeological conditions leading to the corrosion and deterioration of pre-cast segmental concrete linings (case of Zagros tunnel), Geotech. Geol. Eng. 37 (5) (2019) 3961–3983.
[2] R. Yin, C. Zhang, Q. Wu, B.C. Li, H. Xie, Damage on lining concrete in highway tunnels under combined sulfate and chloride attack, Front. Struct. Civ. Eng. 12 (3) (2018) 331–340.
[3] M. Sumer, Compressive strength and sulfate resistance properties of concretes containing Class F and Class C fly ashes, Constr. Build. Mater. 34 (2012) 531–536.
[4] Q.Y. Dong, Y.H. Zhang, L.P. Feng, D.B. Jin, Experimental research of sulfate corrosion resistance of fresh concrete with fly ash, Adv. Mater. Res. 772 (2013) 109–116.
[5] Fethullah Canpolat, Sulfate resistance of mortars containing silica fume and pozzolan, Constr. Mater. 165 (2) (2012) 65–72.
[6] J.S. Yang, P.M. Wang, X.H. Li, X. Yang, Sulfate attack resistance of air-entrained silica fume concrete under dry-wet cycle condition, J. Wuhan. Univ. Technol. (Sci. Technol.) 31 (04) (2016) 857–864.
[7] S. Ogawa, T. Nozaki, K. Yamada, H. Hirao, R.D. Hooton, Improvement on sulfate resistance of blended cement with high alumina slag, Cem. Concr. Res. 42 (2) (2012) 244–251.
[8] X.C. Yan, L.H. Jiang, M.Z. Guo, Y.J. Chen, Z.J. Song, R. Bian, Evaluation of sulfate resistance of slag contained concrete under steam curing, Constr. Build. Mater. 195 (2019) 231–237.
[9] H. Zhou, B. Jia, H. Huang, Y. Mou, Experimental study on basic mechanical properties of basalt fiber reinforced concrete, Materials 13 (6) (2020) 1362.
[10] M. Nematzadeh, S. Fallah-Valukolaee, Erosion resistance of high-strength concrete containing forta-ferro fibers against sulfuric acid attack with an optimum design, Constr. Build. Mater. 154 (2017) 675–686.
[11] J. Yang, B.C. Chen, C. Nuti, Influence of steel fiber on compressive properties of ultra-high performance fiber-reinforced concrete, Constr. Build. Mater. 302 (10) (2021), 124104.
[12] A. Sumathi, D. Elavarasi, K.S.R. Mohan, Performance of high strength steel fiber reinforced concrete subjected to flexure and impact loadings, Rev. Rom. Mater. 51 (2) (2021) 256–263.
[13] M.T. Marvila, H.A. Rocha, A.R.G. De Azevedo, H.A. Colorado, J.F. Zapata, C.M.F. Vieira, Use of natural vegetable fibers in cementitious composites: concepts and applications, Innov. Infrastruct. Solut. 6 (3) (2021) 180.
[14] A. Azevedo, P. De Matos, M. Marvila, R. Sakata, L. Silvestro, P. Gleize, J. De Brito, Rheology, hydration, and microstructure of portland cement pastes produced with ground açaí fibers, Appl. Sci. 11 (7) (2021) 3036.
[15] A.R.G. De Azevedo, M.T. Marvila, B.A. Tayeh, D. Cecchin, A.C. Pereira, S.N. Monteiro, Technological performance of açaí natural fiber reinforced cement-based mortars, J. Build. Eng. 33 (2021), 101675.
[16] A.R.G. De Azevedo, S. Klyuev, M.T. Marvila, N. Vatin, N. Alfimova, T.E.S. De Lima, R. Fediuk, A. Olisov, Investigation of the potential use of curauá fiber for reinforcing mortars, Fibers 8 (11) (2020) 1–13.
[17] M. Khan, M. Cao, C. Xie, M. Ali, Effectiveness of hybrid steel-basalt fiber reinforced concrete under compression, Case Stud. Constr. Mater. 16 (2022), e00941.
[18] B. Liu, X. Zhang, J. Ye, X. Liu, Z. Deng, Mechanical properties of hybrid fiber reinforced coral concrete, Case Stud. Constr. Mater. 16 (2022), e00865.
[19] B. Ali, S.S. Raza, I. Hussain, M. Iqbal, Influence of different fibers on mechanical and durability performance of concrete with silica fume, Struct. Concr. 22 (1) (2020) 318–333.
[20] B. Ali, S.S. Raza, R. Kurda, R. Alyousef, Synergistic effects of fly ash and hooked steel fibers on strength and durability properties of high strength recycled aggregate concrete, Resour. Conserv. Recycl. 168 (2021), 105444.
[21] N. Banthia, R. Gupta, Hybrid fiber reinforced concrete (HyFRC): fiber synergy in high strength matrices, Mater. Struct. 37 (10) (2004) 707–716.
[22] S.G. Chasioti, F.J. Vecchio, Shear behavior and crack control characteristics of hybrid steel fiber-reinforced concrete panels, Acids Struct. J. 114 (1) (2017) 209–220.
[23] M.B. Bankir, U.K. Sevim, Performance optimization of hybrid fiber concretes against acid and sulfate attack, J. Build. Eng. 32 (3–4) (2020), 101443.
[24] Y.Y. Hou, Study on the mechanical and corrosion resistance of hybrid fiber reinforced concrete, J. Funct. Mater. 51 (11) (2020) 11116–11120.
[25] C.Q. Wang, K.R. Wu, Research on the hybrid effect of different geometrical size hybrid fiber reinforced concrete, J. Build. Mater. 8 (3) (2005) 250–255.
[26] N.H. Liang, X.R. Liu, J. Sun, Experimental study of compression for multi-scale polypropylene fiber concrete, Appl. Mech. Mater. 174–177 (2012) 1584–1588.
[27] N.H. Liang, X.R. Liu, J. Sun, Experimental study of splitting tensile for multi-scale polypropylene fiber concrete, Adv. Mater. Res. 450–451 (2012) 168–173.
[28] N.H. Liang, X.R. Liu, J. Sun, Experimental study of crack resistance for multi-scale polypropylene fiber reinforced concrete, J. China Coal Soc. 37 (08) (2012) 1304–1309.
[29] N.H. Liang, J.F. Dai, X.R. Liu, Z.L. Zhong, Experimental study on the fracture toughness of concrete reinforced with multi-size polypropylene fibers, Mag. Concr. Res. 71 (9) (2019) 468–475.
[30] Z.Q. Guo, Experimental Study on the Impermeability of Multi-Scale Polypropylene Fiber Concrete, Chongqing University, 2018.
[31] China code DL/T5330-2015, Code for Mix Design of Hydraulic Concrete, China Electricity Council, China, 2015.
[32] China standard GB/T 50080-2016, Standard for Test Method of Performance on Ordinary Fresh Concrete, Ministry of Housing and Urban-Rural Development of the People's Republic of China, China, 2016.
[33] J.M. Gao, Z.X. Yu, L.G. Song, T.X. Wang, Durability of concrete exposed to sulfate attack under flexural loading and drying-wetting cycles, Constr. Build. Mater. 39 (2013) 33–38.
[34] J.B. Wang, D.T. Niu, Influence of freeze-thaw cycles and sulfate corrosion resistance on shotcrete with and without steel fiber, Constr. Build. Mater. 122 (2016) 628–636.
[35] Z.Y. Zhang, X.G. Jin, W. Luo, Long-term behaviors of concrete under low-concentration sulfate attack subjected to natural variation of environmental climate conditions, Cem. Concr. Res. 116 (2019) 217–230.
[36] S.F. Dong, B.G. Han, X. Yu, J.P. Qu, Constitutive model and reinforcing mechanisms of uniaxial compressive property for reactive powder concrete with super-fine stainless wire, Compos. Part B: Eng. 166 (2019) 298–309.
[37] L. Gan, J. Wu, Z.Z. Shen, X.W. Feng, Deterioration law of basalt fiber reinforced concrete under sulfate attack and dry-wet cycle, China Civ. Eng. J. 54 (11) (2021) 37–46.
[38] Y. Zhou, S. You, H.G. Ji, B.L. Chen, C.L. Song, Mechanical properties of macrosynthetic fibre-reinforced concrete exposed to sulfate attack, Emerg. Mater. Res. 6 (1) (2017) 1–9.
[39] M. Santhanam, Studies on Sulfate Attack: Mechanisms, Test Methods, and Modeling, Indian Institute of Technology Madras, 2001.

[40] Z.Y. Zhang, Mesoscopic Erosion Mechanism and Shear Properties of Shotcrete Materials Under Sulfate-Containing Environments, Chongqing University, 2019.
[41] N.H. Liang, X.R. Liu, J. Sun, Uniaxial tensile test of multi-scale polypropylene fiber reinforced concrete, J. Chongqing Univ. 35 (06) (2012) 80–84.
[42] C.M. Meng, W.Z. Li, L.C. Cai, X.G. Shi, Experimental research on durability of high-performance synthetic fibers reinforced concrete: resistance to sulfate attack and freezing-thawing, Constr. Build. Mater. 262 (14) (2020), 120055.
[43] D.M. Carlesso, S.H.P. Cavalaro, A.D.L. Fuente, Flexural fatigue of pre-cracked plastic fibre reinforced concrete: experimental study and numerical modeling, Cem. Concr. Compos. 115 (2021), 103850.
[44] Z.W. Wu, H.Z. Lian, High Performance Concrete, China Railway Publishing House, 1999.
[45] H. Tian, Study on Sulfate Transmission-Degradation Mechanism of Concrete Under Long-Term Soaking, Shenzhen University, 2015.
[46] T. Ikumi, S.H.P. Cavalaro, I. Segura, A. Aguado, Alternative methodology to consider damage and expansions in external sulfate attack modeling, Cem. Concr. Res. 63 (2014) 105–116.
[47] D. Krajcinovic, M. Basista, K. Mallick, D. Sumarac, Chemo-micromechanics of brittle solids, J. Mech. Phys. Solids 40 (5) (1992) 965–990.
[48] N. Barovsky, R. Blagoeva, M. Mironova, N. Petrov, Modelling of sulfate ion diffusion in cement stone, Mater. Eng. 3 (3) (1992) 365–376.